Journal of the European Ceramic Society 43 (2023) 4517–4529

Contents lists available at ScienceDirect

Journal of the European Ceramic Society

journal homepage: www.elsevier.com/locate/jeurceramsoc

Tuning the mechanical and thermal properties of (MgNiCoCuZn)O by intelligent control of cooling rates

Varatharaja Nallathambi [a,1], Lalith Kumar Bhaskar [a,b,1], Di Wang [c], Aleksandr A. Naberezhnov [d], Sergey V. Sumnikov [e], Emanuel Ionescu [f,g], Ravi Kumar [a,b,*]

[a] Laboratory for High Performance Ceramics, Department of Metallurgical and Materials Engineering, Indian Institute of Technology Madras (IIT Madras), Chennai 600036, India
[b] Ceramic Technologies Group, Centre of Excellence in Materials and Manufacturing for Futuristic Mobility, Indian Institute of Technology Madras (IIT Madras), Chennai 600036, India
[c] Institute of Nanotechnology and Karlsruhe Nano Micro Facility (KNMFi), Karlsruhe Institute of Technology, Eggenstein-Leopoldshafen, Germany
[d] Laboratory of Neutron Research, Ioffe Institute, St.-Petersburg, Russia
[e] Frank Laboratory of Neutron Physics, Joint Institute for Nuclear Research, Dubna, Russia
[f] Institute for Materials Sciences, Technical University of Darmstadt, Darmstadt 64287, Germany
[g] Fraunhofer Institution for Materials Recycling and Resource Strategies (Fraunhofer IWKS), Brentano str. 2a, D-63755 Alzenau, Germany

ARTICLE INFO

Keywords:
Entropy stabilized oxides
Heat-treatment
Phase stability
CuO nucleation

ABSTRACT

The possibility of altering the phase equilibria of multicomponent oxide systems through precise control of configurational entropy has opened a platform with unlimited possibilities to fine-tune material properties. The current work is aimed at tailoring the mechanical and thermal properties of (MgNiCoCuZn)O by an intelligent design of constituent phase structure resulting from controlled cooling from the stabilization temperature. Based on the cooling rates, the amount of CuO nucleation was found to vary between 5.4 and 12.3 wt%, along with a corresponding decrease in Cu^{2+} content in the matrix. It was observed that with the decrease in Cu^{2+} ion concentration in the matrix, the Young's modulus and hardness increased by 33% and 26%, respectively, along with a corresponding decrease in the coefficient of thermal expansion by 15%. Similarly, an increased nucleation of CuO precipitates led to the improvement of fracture toughness of the material by 15%, while its thermal conductivity remained unaltered.

1. Introduction

A quest for advanced material systems with superior properties that can fulfil the demands of modern technological trends still poses an imposing challenge in the field of materials science. The possibility of altering the phase stability of solid solutions through precise control of configurational entropy paves way for the development of new classes of high entropy materials. The concept of high entropy materials was initially confined to the world of metals and their alloys and has now been extended to non-metallic systems [1–5]. The first equimolar multicomponent oxide system (MgNiCoCuZn)O was synthesized and reported by Rost et al. as entropy stabilized oxides (ESO)[6], which are now commonly known as high entropy oxides (HEO). The multi-cation transition metal oxide system (MgNiCoCuZn)O still remains interesting since the system reveals characteristics of very low thermal conductivity [7,8], is elastically isotropic in nature [9], and exhibits high dielectric constants over a wide range of frequencies [10]. Furthermore, (MgNiCoCuZn)O was found to be catalytically active and extremely stable in the high-temperature oxidation of CO [11], a suitable candidate for the two-step thermochemical water splitting process at reduced temperatures [12], and a potential material for reversible energy storage [13] due to its high Li-ion conductivity [14]. The presence of multiple cations in the sublattice of ESO gives rise to novel and exciting properties resulting from interactions between one another, which is the essence of the 'cocktail effect'. Despite the impressive properties, a thorough understanding of the factors influencing such material behavior is necessary for maximizing the performance of these materials.

There have been extensive studies related to the phase evolution and

* Corresponding author at: Laboratory for High Performance Ceramics, Department of Metallurgical and Materials Engineering, Indian Institute of Technology Madras (IIT Madras), Chennai 600036, India.
E-mail address: nvrk@iitm.ac.in (R. Kumar).
[1] Equal contribution.

https://doi.org/10.1016/j.jeurceramsoc.2023.03.016
Received 9 October 2022; Received in revised form 5 March 2023; Accepted 7 March 2023
Available online 9 March 2023

stability of this multicomponent system as a function of temperature, pressure and composition. Earlier studies were directed towards understanding the effects of an additional cation in the 5 component system [10,15,16] and also the effects of local distortion due to the Jahn-Teller effect by the Cu^{2+} ions on the phase stability [15,17–20]. Further studies reported the effects of high pressure (> 6 GPa) on the phase stability [21] and on the deformation behavior of this 5 component system [22,23]. Extensive studies were also carried out to understand the densification behavior of this entropy stabilized oxide system and its effect on mechanical and thermal properties [7,24]. Also, the variation in morphology and phase fraction of the secondary phases that is altered by varying the heat-treatment parameters have been reported [24–26]. However, no reports exist in the literature exploring the effect of nucleation & role of secondary phases on the thermal and mechanical properties of (MgNiCoCuZn)O. The feasibility of controlling the process and nature of the nucleation of a secondary phase in a multicomponent system provides an additional degree of freedom in tunability of the material properties.

In this work, the interrelation between the factors such as thermal treatment and secondary phase nucleation and their role in the thermal and mechanical properties is explored and systematically studied. The first portion of the paper reports the results obtained from the heat treatment experiments of the multicomponent oxide system [(MgNiCoCuZn)O] and the subsequent variation in the mechanical and thermal properties. Followed by which the variation in the observed properties is explained using neutron diffraction, EELS spectroscopy, multivariate statistical analysis (MSA) on a STEM-EDX mapping and molecular dynamics simulation.

2. Experimental details

2.1. Synthesis and heat-treatment

Entropy stabilized oxides (MgNiCoZnCu)O were synthesized by solution combustion synthesis (SCS) process using the nitrates of respective metals, i.e., magnesium nitrate hexahydrate $Mg(NO_3)_2{\cdot}6\ H_2O$ (Alfa Aesar), nickel nitrate hexahydrate $Ni(NO_3)_2{\cdot}6\ H_2O$ (Alfa Aesar), cobalt nitrate hexahydrate $Co(NO_3)_2{\cdot}6\ H_2O$ (Alfa Aesar), copper nitrate hemipentahydrate $Cu(NO_3)_2{\cdot}2.5\ H_2O$ (Alfa Aesar), zinc nitrate hexahydrate $Zn(NO_3)_2{\cdot}6\ H_2O$ (Alfa Aesar) and glycine $C_2H_5NO_2$ – 99% (Alfa Aesar) as fuel. The synthesis procedure can be found elsewhere [19]. The as-synthesized powders were calcined in a tubular furnace at 1000 °C for 2 h, followed by quenching in air (referred to as *air quenched* in the results). The solution combustion synthesized powders were consolidated into solid pellets using spark plasma sintering (Sumitomo Coal Mining Co. Ltd, Japan) in vacuum. The sintering process was carried out in a graphite die of diameter 15 mm. The graphite die was filled with the SCS powder separated by a thin graphite foil to avoid sticking of the sample with the punch after the sintering process. The sintering process was carried out at 1050 °C with a holding time of 5 min and at a constant heating rate of 100 °C/min under a pressure of 50 MPa for all the samples. Heat-treatment studies were carried out in a tubular furnace at a heating rate of 5 °C/min and a holding time of 2 h in air atmosphere followed by varying cooling rates (5 °C/min, 2 °C/min & 1 °C/min). The samples treated with different cooling rates are referred to as *slow cooled* samples and the samples treated with no set cooling rate and just left in the furnace to cool are referred to as *furnace cooled* samples.

2.2. Structural characterization

X-ray diffraction was carried out for powders as well as for the sintered and heat-treated pellets using Bruker D8 Discover (Germany) with 2θ ranging from 10° to 90°, step size of 0.01° and a scan speed of 1 s/step. The accelerating voltage and current were kept at 30 kV and 30 mA. Phase analysis and Rietveld refinement of the diffraction data were done using X′pert HighScore Plus software.

The morphological features and elemental composition of the sintered and heat-treated pellets were analyzed using SEM, Thermofischer - Apreo S (USA) and FEI Quanta 400 (USA) coupled with energy-dispersive X-ray spectroscopy (EDS) analysis using Bruker X Flash (Germany). The atomic fractions were determined via averaging the EDS data obtained from over 10 spots.

High-angle annular dark-field (*HAADF*) scanning transmission electron microscopy (STEM) *imaging* was carried out for the sintered and heat-treated pellets using 200 kV FEI Tecnai F20 ST (USA). STEM-EDX and STEM-EELS were carried out on a Thermofischer Scientific Themis Z transmission electron microscope, operating at 300 kV accelerating voltage and equipped with probe and image correctors, superX EDX detector and Gatan image filter (GIF) continuum 970. 4D-STEM microprobe diffraction was performed using the same TEM using Gatan Oneview camera with STEMx system. The sample was prepared by slicing a thin cross-section (less than 0.7 mm in thickness) from the pellet using a low-speed diamond cutting machine from Struers Ltd, USA. The thickness of the sliced portion was progressively reduced to less than 0.1 mm by polishing with SiC emery sheets. A 3 mm disc was prepared from the thinned down slice using an ultrasonic disc cutter from Gatan Inc.,(USA). A disc of 3 mm in diameter was thinned further such that it was electron transparent using an ion miller from Gatan Inc., (USA).

Neutron diffraction was carried out at room temperature for the powder samples in the time-of-flight (TOF) High Resolution Fourier Diffractometer (HRFD) mode on the pulsed neutron reactor IBR-2 in the Joint Institute for Nuclear Research (JINR) (Dubna, Russia) [27]. The measurement time for each sample was 8 h. The working distance was from d = 0.6–2.4 Å. The resolution (FWHM/d) function changed from 0.0021 at d = 0.6 Å to 0.0017 at d = 2.4 Å. All spectra were treated using the FullProf program. Elastic peaks were described by a special function, which is a convolution of pseudo-Voigt with back-to-back exponential functions [28].

The Raman spectra of powder samples were carried out using a LabRAM HR800 Raman spectrometer from Horiba Jobin-Yvon (Japan) equipped with an Olympus BX41 microscope having an objective lens magnification of 50 × . The samples were excited with a He-Ne laser source of 632 nm wavelength and signals were obtained in the range of 200 cm^{-1} to 2400 cm^{-1} using a 5 mW power supply.

The electron paramagnetic resonance spectrometry of the powder samples was performed using JEOL JES FA200 (USA) instrument at room temperature at X band frequency of 9.65 GHz with a sensitivity of 7×10^9 spins/0.1 mT. The recorded intensity values were plotted against the magnetic field (G) and the corresponding g values were obtained by simulation of EPR data using EasySpin software 5.0 [29].

2.3. Mechanical characterization

An ultrasonic resonant frequency testing method (KEYSIGHT Technologies, USA) was used to measure the Poisson's ratio and Young's modulus of the sintered and heat-treated ESO samples. Poisson's ratio and Young's modulus were calculated using the longitudinal and shear velocities measured from the ultrasonic testing using the following equations.

$$\mu = \frac{1 - 2\left(\frac{V_s}{V_l}\right)^2}{2 - 2\left(\frac{V_s}{V_l}\right)^2} \tag{1}$$

$$E = \frac{\rho V_l^2 (1+\mu)(1-2\mu)}{(1-\mu)} \tag{2}$$

where, μ is the Poisson's ratio, E is the Young's modulus, V_l is the longitudinal velocity, V_s is the shear velocity and ρ is the density of the material.

Nanoindentation for the sintered and heat-treated ESO samples was

carried out using Hysitron Inc., USA, with a standard Berkovich indenter with a load of 10 mN. Loading, unloading and dwell time for the indentation was set constant to a value of 10 s for all the samples, which resulted in a trapezoidal load function. The reduced elastic modulus (E_r) was determined using the Oliver–Pharr method.

$$\frac{1}{E_r} = \frac{1-\nu^2}{E} + \frac{1-\nu_i^2}{E_i} \tag{3}$$

where, E and ν are the elastic modulus and Poisson's ratio of the sample while E_i and ν_i are the elastic modulus and Poisson's ratio of the Berkovich indenter respectively. The Young's modulus and hardness values were calculated from an average of 10 indents for each sample.

To determine the fracture toughness in mode-I of the sintered and heat-treated samples, a load of 1 kg was applied with a dwell time of 10 s to indent the sample surface in order to generate cracks using a Vickers micro-hardness tester (Model: 420 MVD, Wolpert Wilson Instruments, USA). The fracture toughness values were calculated using the crack opening displacement (COD) method by visualizing the radial cracks formed at the indents over the sample surface in the scanning electron microscope (SEM). Half of the crack opening displacement (u) is plotted as a function of distance from the crack tip, which is also known as the crack interface coordinate. The crack profile is then fitted as per the following equation to calculate the fracture toughness value.

$$u(x) = \frac{K_{tip}}{E}\sqrt{\frac{8}{\pi}}x^{0.5} + Ax^{1.5} + Bx^{2.5} \tag{4}$$

where, K_{tip} is the stress intensity factor at the crack tip, which is equal to K_{IC} under equilibrium conditions, E is the elastic modulus and x is the distance from the crack tip.

2.4. Thermal characterization

The thermal expansion behavior of the sintered and heat-treated samples was studied using a NETZSCH Dil 402 Expedis (Germany) dilatometer. The prepared samples were heated to 1000 °C at a constant heating rate of 10 °C/min in air atmosphere to record its change in length in the linear direction. The average linear coefficient of thermal expansion values over a temperature range was calculated from the first differential of the dL/L_o vs. temperature curve obtained during the measurement.

Thermal diffusivity measurements were performed using Linseis LFA 1250, Germany. The sintered pellets were cut into thin discs of 10 mm in diameter and 2 mm in thickness for the measurement. The diffusivity values were recorded over a temperature range of RT to 1000 °C. The sintered samples' specific heat capacity (Cp) measurements were performed using NETZSCH DSC 204 F1 PHOENIX, Germany. The samples were heated in an alumina crucible to 500 °C at a heating rate of 10 °C/min in static airflow. The thermal conductivity values were calculated as per the following equation.

$$\kappa(T) = \alpha(T) \times Cp(T) \times \rho \tag{5}$$

where, κ is the thermal conductivity, α is the thermal diffusivity, C_p is the specific heat capacity and ρ is the density of the material.

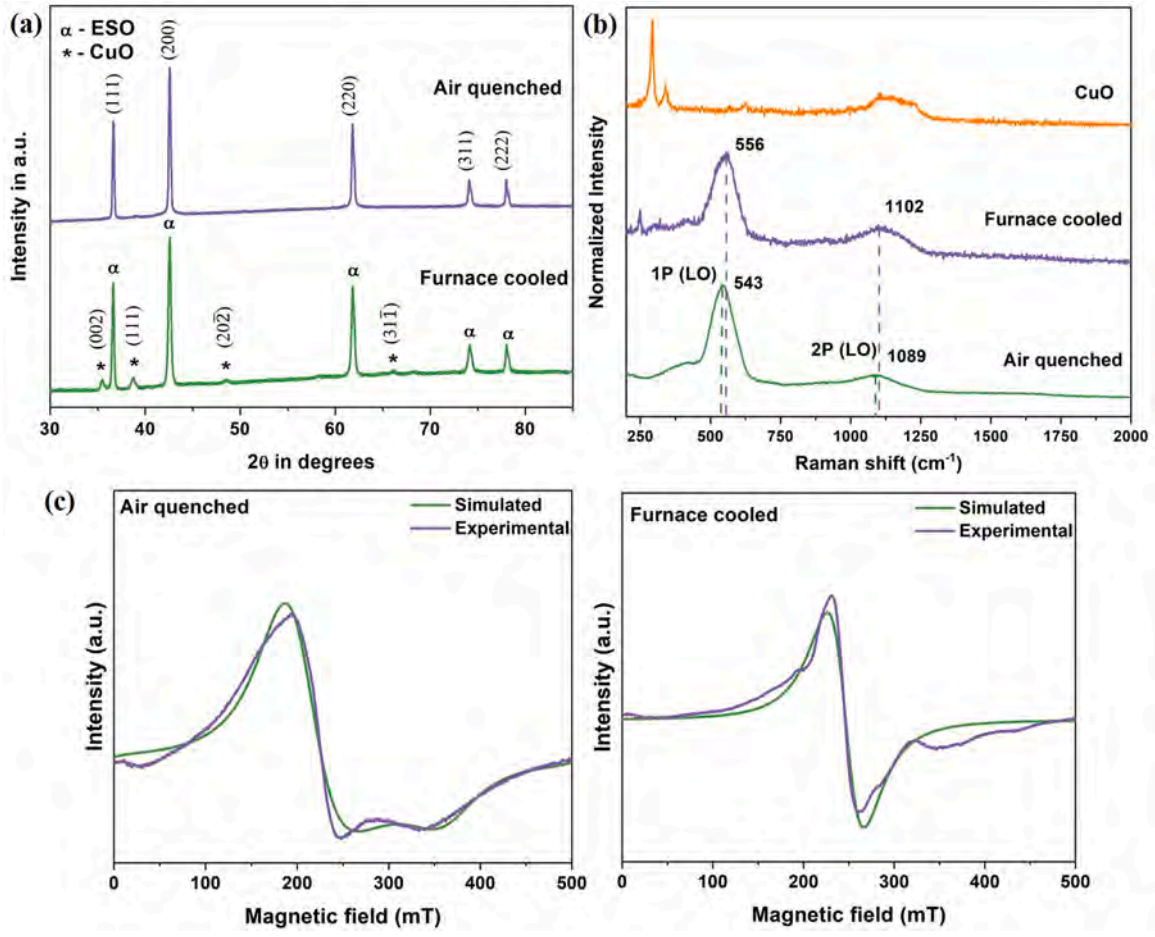

Fig. 1. **(a)** shows the X-ray diffractograms **(b)** Raman spectra and **(c)** X-band EPR spectra of the air quenched and furnace cooled (MgNiCoCuZn)O ESO powders. Also, shown in **(b)** is the Raman spectra of commercial CuO powder.

3. Results

3.1. Nucleation of secondary phases – effects of cooling rate

3.1.1. Powder ESO samples

Fig. 1(a) shows the X-ray diffractograms of a single-phase rocksalt structure obtained by heat-treatment of the solution combustion synthesized powders at 1000 °C for 2 h, followed by quenching it to room temperature. Also, shown in Fig. 1(a) is the diffractogram of the SCS synthesized powders heat-treated at 1000 °C for 2 h followed by *furnace cooling*. Furnace cooling always inevitably results in the nucleation of CuO precipitates. However, the transformation from a multi-phase mixture to a single phase is reversible. The nucleated CuO precipitates possess a monoclinic crystal structure, and additional spectroscopic analysis was done to confirm CuO nucleation.

Raman spectroscopy performed on the ESO sample revealed the peaks corresponding to the rocksalt structure ESO, as shown in Fig. 1(b). The peak near 543 cm^{-1} was assigned to 1 P LO mode. The peak at 1089 cm^{-1} was attributed to the 2 P LO mode [30]. The assigned vibrations of the Raman spectra were based on a structure that possesses a similar symmetry to the rocksalt type ESO such as NiO and CoO. Raman spectroscopy performed on the *furnace cooled* ESO sample confirmed the

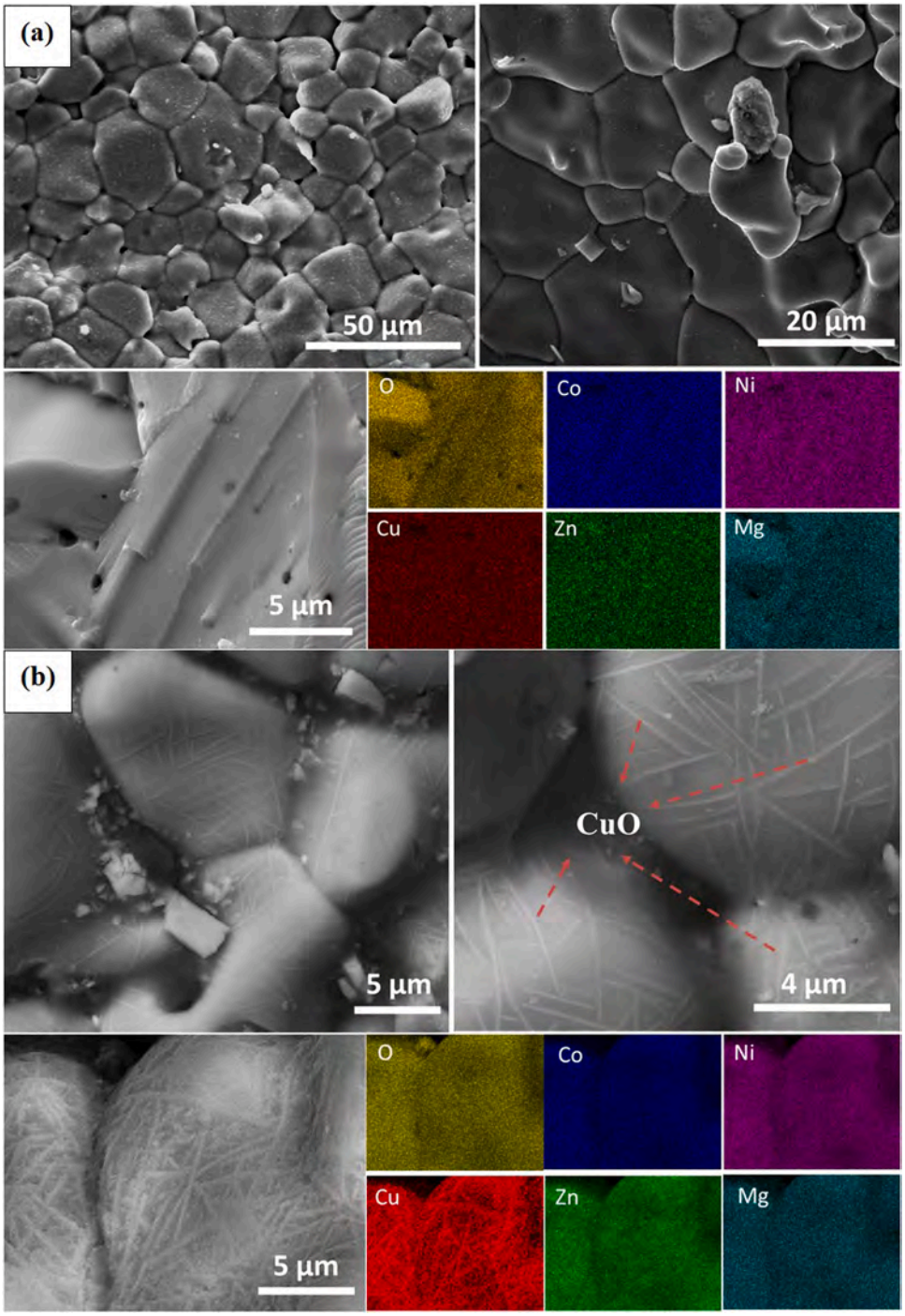

Fig. 2. **(a)** shows the SEM micrographs and elemental mapping of the SPS sintered single-phase [(MgNiCoCuZn)O] ESO sample and **(b)** shows the SEM micrographs and elemental mapping of the furnace cooled SPS sintered sample. CuO precipitates can be identified in the furnace cooled sample.

presence of CuO precipitates which is compared with the Raman spectra of the commercial CuO powder sample. However, in comparison with the *air quenched* sample, the *furnace cooled* ESO sample exhibited a blue shift for the peaks at 556 and 1102 cm^{-1}. The shift in peaks could be attributed to the lowering of the local distortion in the matrix resulting from the nucleation of CuO. To further confirm the relaxation of local distortion, electron paramagnetic resonance (EPR) spectroscopy was done. Fig. 1(c) shows the X-band EPR spectra of the air quenched and furnace cooled ESO samples. The EPR signal of the *air quenched* ESO (stabilized) sample is distorted with the simulated g values of g(x) = 3.30, g(y) = 3.31 and g(z) = 1.88 indicating the anisotropy in the crystal symmetry and a deviation from an ideal rocksalt structure [31]. In contrast, the signal from the *furnace cooled* ESO sample is near isotropic with g(x) = 2.739, g(y) = 2.739 and g(z) = 2.737 confirming the reduction in the lattice distortion due to the nucleation of CuO.

3.1.2. Sintered ESO samples

The ESO powders were consolidated to pellets using spark plasma sintering and subjected to similar heat-treatment conditions as the powder samples to study the mechanical and thermal properties. The relative density measured using the Archimedes principle resulted in a value of 6.05 g/cm^3, which is 99% of the theoretical density (6.137 g/cm^3) of [(MgNiCoCuZn)O] ESO. Fig. 2(a) shows the SEM micrographs and elemental mapping of the single-phase SPS sintered sample. The micrographs reveal a pore-free well-sintered microstructure with an average grain size of 14 ± 1.5 μm. Elemental mapping using SEM confirms the uniform distribution of elements in the matrix. Table 1 gives an average EDS compositional analysis of the various elements present in the lattice in atomic percentage. No local clustering or segregation was observed.

Similar to powder samples, *furnace cooling* results in the nucleation of CuO in sintered samples. Fig. 2(b) shows the SEM micrographs of the *furnace cooled* ESO sample containing CuO precipitates and its respective elemental mapping. The CuO nucleating from the matrix, precipitates in a needle shape morphology. The elemental mapping confirms that the nucleated phase is CuO.

The aforementioned experiments make it clear that CuO nucleation is inevitable when the sample is *furnace cooled*. Further experiments with controlled cooling rates were carried out to understand the CuO nucleation behavior. Fig. 3 shows the X-ray diffractograms of the *slow cooled* samples with different cooling rates of 5, 2 and 1 °C/min. Experiments were restricted to the aforementioned cooling rates since the nucleation of CuO is suppressed at faster cooling rates. Also, the cooling rate of 5 °C/min mimics the furnace cooling condition. The amount of CuO nucleated increases with a decrease in the cooling rate as the intensity of the CuO peaks is found to increase gradually. Particularly, the $(20\bar{2})$ peak of CuO starts to appear for the 2 °C/min furnace cooled sample and its intensity increases further for 1 °C/min furnace cooled sample.

For further investigation, four samples with different heat-treatment conditions (quenched, slow cooled at 5, 2 and 1 °C/min) were chosen and are compared with their CuO-free 4-component ESO counterpart. It was reported that Cu^{2+} ions in (MgNiCoCuZn)O system experience Jahn-Teller distortion [18] and for the system to remain as a single phase, there is a necessity to create a certain fraction of oxygen vacancies, which overcomes the tensile state of stress around the Cu^{2+} ions in the lattice induced by Jahn-Teller distortion [19]. Therefore, it was intuitive to study and contrast the mechanical and thermal properties obtained for the varying *slow cooled* ESO samples with the CuO-free

Table 1
Average EDS compositional analysis of various elements present in the lattice in atomic percentage.

Element	Oxygen	Magnesium	Nickel	Cobalt	Copper	Zinc
Atomic %	45.4 ± 3.5	11.4 ± 1.4	10.9 ± 0.8	11.1 ± 0.7	10.8 ± 0.9	10.3 ± 0.8

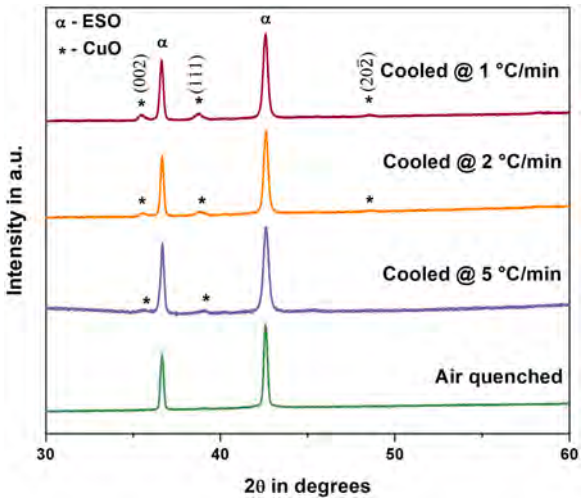

Fig. 3. shows the X-ray diffractograms of the ESO stabilized sample and slow cooled samples at different cooling rates (5, 2 and 1 °C/min).

4-component ESO counterpart [(MgNiCoZn)O], in which almost no Jahn-Teller distortion effects should be observed. Table 2 shows the sample nomenclature followed in the subsequent sections for the different heat-treated samples with varying cooling rates and the corresponding weight percentage of CuO nucleated that was calculated using Rietveld refinement.

3.2. Variation in mechanical properties

The Young's moduli and Poisson's ratio of the sintered samples are shown in Fig. 4(a) & (b). The measured values for the ESO stabilized sample matched well with the literature reported values [9]. A 33% increase in the modulus value was observed for the 1 °C/min *slow cooled* sample (containing 12.3 wt% CuO nucleated) measured using both techniques and the average standard deviation in modulus is less than ±10 GPa and the apparent increase in modulus with respect to CuO nucleation is beyond the standard deviation. Also, a 26% increase in hardness value and a 6% decrease in Poisson's ratio were observed for the 1 °C/min *slow cooled* sample. For comparison, the measured values for ESO 4 C are also shown in Fig. 4.

Fig. 5(a) shows a representative crack displacement profile of the ESO stabilized sample and the inset shows the SEM image of the crack profile observed. The curve was fitted using Eq. (4) and the fracture toughness values were calculated from the constants obtained. Fig. 5(b) shows the fracture toughness values of the various sintered and *slow cooled* ESO samples. The fracture toughness increased by 15% with the increase in weight% of CuO nucleated from the matrix.

3.3. Variation in thermal properties

The linear thermal expansion behavior of the sintered and heat-treated samples is shown in Fig. 6(a). The average linear coefficient of thermal expansion (CTE) values were calculated between the temperature range of 200–700 °C from the change in length curve. A change in

Table 2
Sample nomenclature followed for the different heat treated ESO samples with varying cooling rates.

Sample nomenclature	Sample details
ESO 5 C	Single-phase stabilized (MgNiCoCuZn)O ESO
ESO SC-5	Slow cooled at 5 °C/min containing **5.4 wt%** of CuO
ESO SC-2	Slow cooled at 2 °C/min containing **8.2 wt%** of CuO
ESO SC-1	Slow cooled at 1 °C/min containing **12.3 wt%** of CuO
ESO 4 C	Single-phase stabilized (MgNiCoZn)O ESO with no CuO

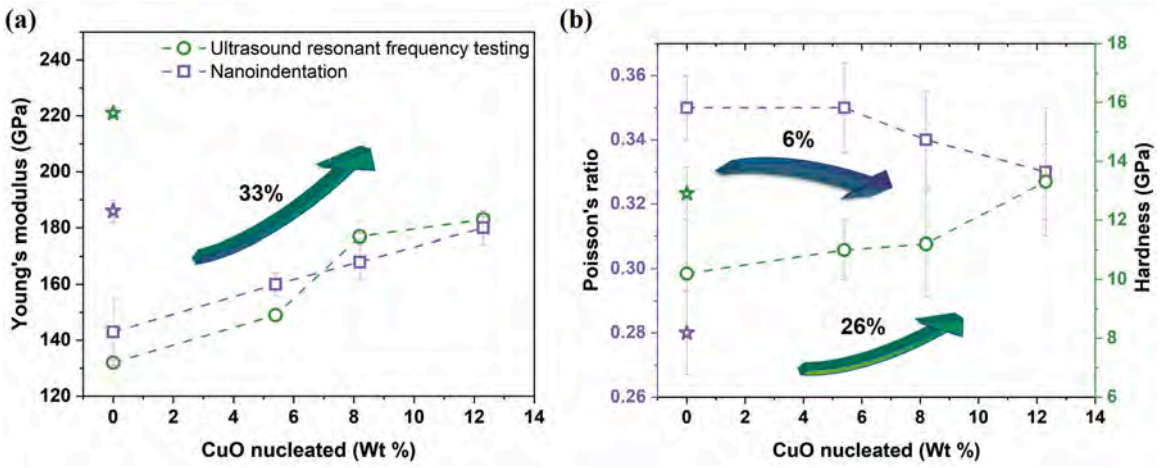

Fig. 4. **(a)** shows the Young's modulus values of the sintered and heat-treated ESO samples measured using ultrasonic resonant frequency testing and nano-indentation **(b)** shows the hardness and Poisson's ratio measured using nanoindentation and ultrasonic resonant frequency testing respectively. For reference the values of ESO 4 C system (no CuO) is represented by a star symbol.

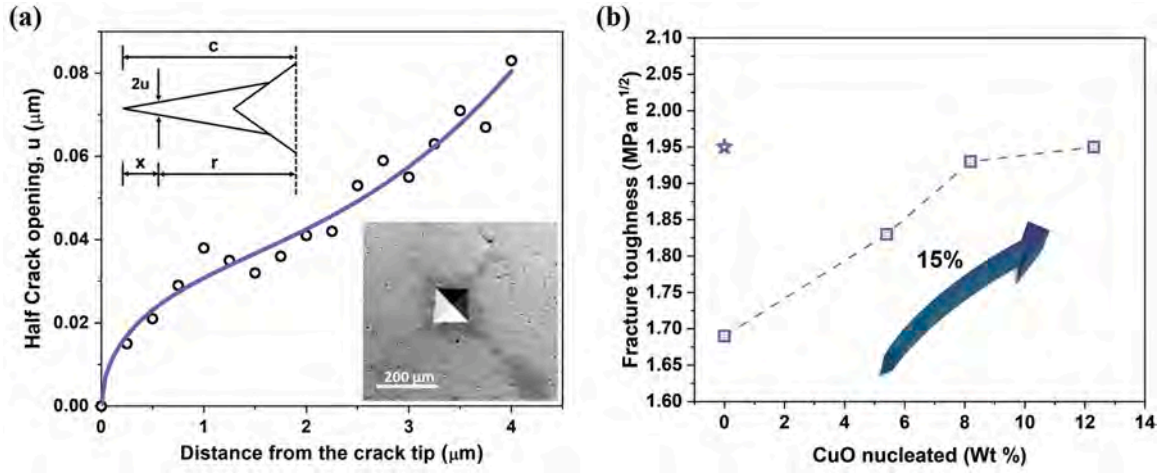

Fig. 5. **(a)** shows a representative crack opening displacement profile of the ESO stabilized sample and **(b)** shows the variation in fracture toughness values of the various sintered and heat-treated ESO samples with different slow cooled conditions compared with ESO 4 C sample represented by the star symbol.

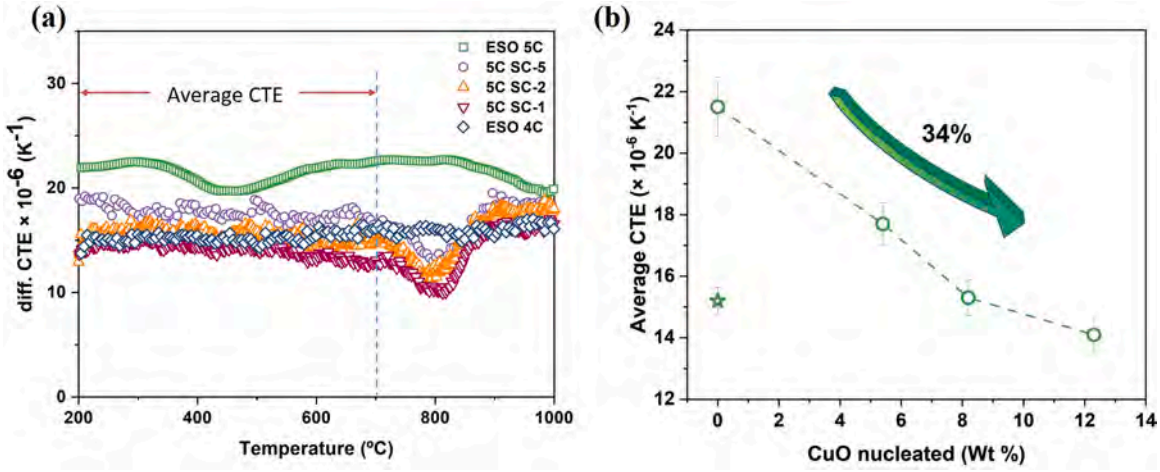

Fig. 6. **(a)** shows the linear thermal expansion behaviour of the sintered ESO samples with different slow cooled conditions and **(b)** shows the average linear CTE values for the respective samples. For reference the value of ESO 4 C system (no CuO) is represented by a star symbol.

the slope of the thermal expansion curve was observed above 700 °C in the *slow cooled* samples indicating the dissolution of nucleated CuO back into the matrix. The average CTE values measured in the temperature range of 200–700 °C are shown in Fig. 6(b). The average CTE value for the ESO stabilized sample is 21.5 × 10^{-6} K^{-1} and the CTE values for the 1 °C/min slow cooled sample (containing 12.3 wt% CuO nucleated) decreased by 34%. It has to be pointed out that the average standard deviation in CTE values are less than ±1.5 × 10^{-6} K^{-1} and the apparent decrease in CTE with respect to CuO nucleation is beyond the standard deviation. For comparison, the measured values for ESO 4 C are also shown in Fig. 6(b).

The variation in the thermal conductivity as a function of temperature over the range of RT to 500 °C is shown in Fig. 7(a). The measured thermal conductivity value of 2.8 $Wm^{-1}K^{-1}$ for the ESO stabilized sample matched well with the literature reported value [7]. As shown in Fig. 7(b), there was not much variation in the average thermal conductivity value with the increase in weight% of CuO nucleated from the matrix. The variation in thermal conductivity with an increase in CuO nucleation is within the average standard deviation value of ±0.2 $Wm^{-1}K^{-1}$. The specific heat capacities for all the systems used for calculating thermal conductivity are shown in supplementary Fig. S1. An average standard deviation of ± 5.9% is observed for the measured specific heat capacity values. In addition, a strong temperature dependency was observed for ESO 4 C samples, which was not the case for other samples.

4. Discussion

From the results, both the mechanical and thermal properties of the ESO system vary with the difference in cooling rates. For the slowest cooling rate, i.e., ESO SC-1, Young's modulus, hardness and fracture toughness of the material increased by 33%, 26% and 15%, respectively, compared to the ESO 5 C sample. At the same time, the Poisson ratio and linear coefficient of thermal expansion decreased by 6% and 34%. Unlike other properties, the material's thermal conductivity did not vary with the variation in cooling rate. Additional neutron diffraction experiments and HRTEM characterization combined with molecular dynamics (MD) simulations were carried out to rationalize the observed results. The following section first discusses the compositional and microstructural changes observed in the system due to slow cooling rates. The scientific reasoning for the observed variation in the properties succeeds later.

4.1. Compositional and microstructural changes in the slow cooled ESO systems

From the results, two interrelated phenomena were observed for the ESO *slow cooled* samples, i.e., with a decrease in cooling rates, CuO was precipitated from the matrix and the matrix composition was approaching more like that of an ESO 4 C system. Neutron diffraction of the *slow cooled* ESO samples was carried out to understand further the variation in crystal structure. The neutron diffraction for the *slow cooled* ESO samples reveals a shift in peaks to higher 2-theta angles with variation in cooling rates. The results are consistent with the X-ray diffraction results, as shown in Fig. 8(a) for (200) diffraction peak. For comparison, the (200) diffraction peak of the ESO 4 C sample is also shown in Fig. 8(a). The corresponding variation in the lattice parameters calculated from the X-ray and neutron diffraction diffractograms for the *slow cooled* ESO samples and ESO 4 C is shown in Fig. 8(b). From the variation in lattice parameter and peak shift, it can be hypothesized that the matrix of the ESO stabilized system tends to become more like an ESO 4 C system with the decrease in cooling rate. To confirm, multivariate statistical analysis (MSA) on a STEM-EDX mapping of the ESO SC-1 sample was carried out. Multivariate statistical analysis (MSA) on a STEM-EDX mapping provides more accurate quantification of the contribution from different components present at each pixel [32]. As shown in Fig. 9, two distinct components were identified in the MSA, corresponding to the matrix and precipitate regions, respectively. The corresponding atom fraction for both the components is provided in Table 3. From the atom fractions of component 1 and component 2, it can be confirmed that there are very few Cu^{2+} cations left in the matrix and also the nucleated precipitate is Cu-rich with an atomic fraction of Cu:O to be 0.94:1. Therefore, the presumption of the matrix transitioning to one similar to ESO 4 C could be confirmed.

The other interrelated effect observed because of the slow cooling is the nucleation of CuO precipitates out of the matrix. HR-TEM studies of the nucleated CuO in the ESO SC-1 sample were carried out to understand the microstructural changes. The average length and thickness of the precipitates are 10 ± 4 μm and 54 ± 17 nm, respectively. The area fraction of the precipitate was calculated to be 15±3%. Fig. 10 shows the electron energy loss spectroscopy (EELS) of the CuO precipitates, where the L2 & L3 edge show typical Cu^{2+} features [33]. Also shown in Fig. 10 are the high-angle annular dark-field imaging (HAADF) and STEM-EDS mapping of the CuO precipitates. From the STEM-EDS mapping, it is clear that the precipitates are Cu-rich. Scanning diffraction imaging was carried out using a microprobe beam (beam size around 1 nm) to determine the orientation relation between the matrix and precipitate.

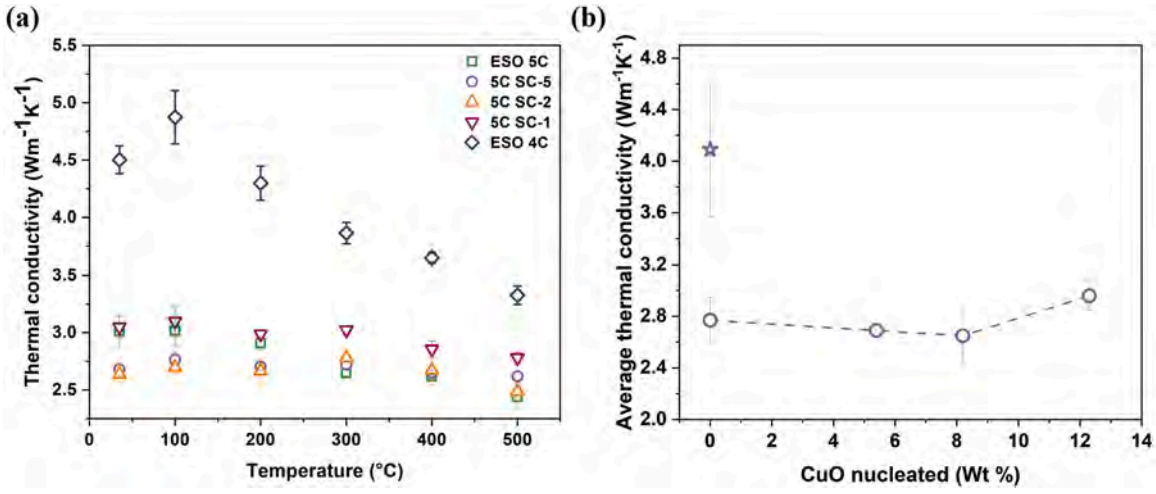

Fig. 7. **(a)** shows the variation in thermal conductivity values with temperature for the sintered ESO samples with different slow cooled conditions and **(b)** shows the average thermal conductivity values for the various samples. For reference the value of ESO 4 C system (no CuO) is represented by a star symbol.

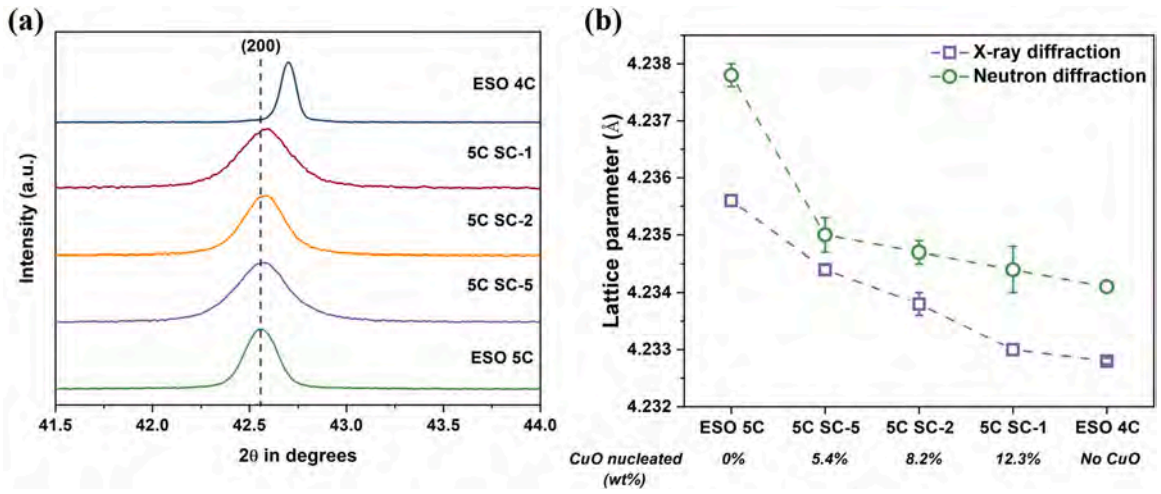

Fig. 8. **(a)** shows the observed peak shift in the (200) peak of the X-ray diffraction pattern and **(b)** shows the variation in lattice parameter calculated using Rietveld refinement from the X-ray and neutron diffraction data.

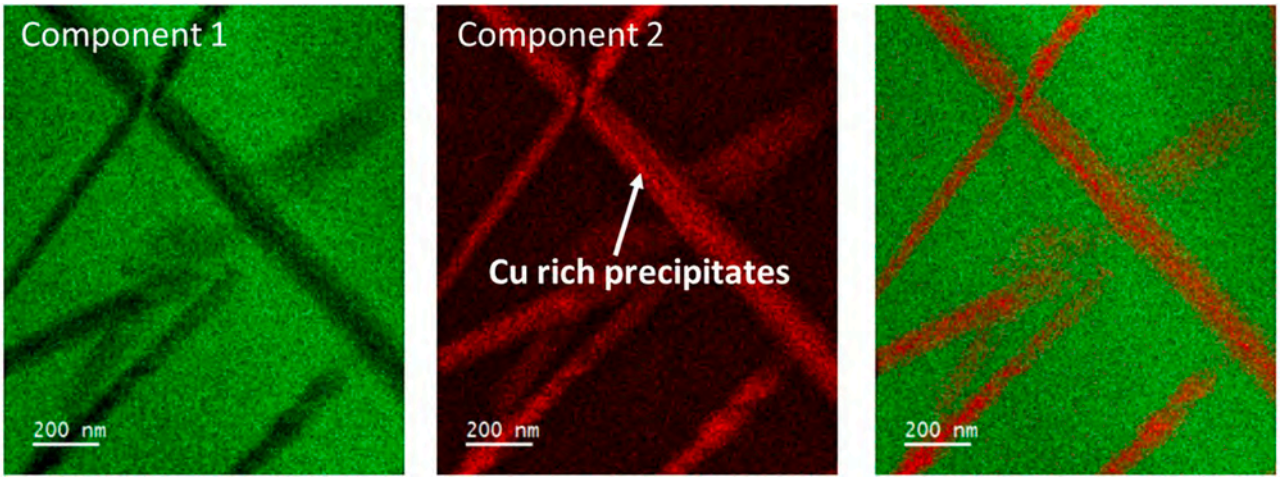

Fig. 9. shows the multivariate statistical analysis (MSA) on a STEM-EDX mapping of the ESO SC-1 sample. Two major components are identified and the corresponding atom fractions of the elements are shown in Table 3.

Table 3
Atom fractions of the elements identified by the multivariate statistical analysis (MSA) on a STEM-EDX mapping of the ESO SC-1 sample.

Component 1						
Element	**Oxygen**	**Magnesium**	**Nickel**	**Cobalt**	**Copper**	**Zinc**
Atomic %	44.49	9.72	14.28	15.77	0.26	15.45
Component 2						
Element	**Oxygen**	**Magnesium**	**Nickel**	**Cobalt**	**Copper**	**Zinc**
Atomic %	46.86	3.15	4.59	1.46	43.67	0.24

Fig. S2 shows the diffraction patterns obtained from the matrix and precipitate along the three different zone axis ([100], [110] & [111]) of the ESO matrix. The diffraction pattern from the three zone axes reveals that the precipitates do not have a simple monoclinic structure of CuO. However, the basic structure of the precipitate could still be identified similar to pure-CuO, given the fact that the major intensive diffraction spots from the precipitates are well correlated to the monoclinic CuO structure. The precipitate could be considered as a superstructure due to its modulation by doping of Ni, Mg and Co cations considering the following, i) the Cu L-edge from the EELS data indicates that the Cu valence state is close to + 2; ii) there are small amounts of Ni, Mg and Co cations distributed in the precipitate as evident from the multivariate statistical analysis; and iii) the Cu:O ratio being slightly lesser than 1.

4.2. *Effect of compositional variation of the matrix on the properties*

4.2.1. *Mechanical properties*

The Young's modulus of the ESO sample increased by 33% with a decrease in the cooling rate. Understanding the variation in Young's modulus should help explain the variation observed in other properties, such as coefficient of thermal expansion and hardness, as all of them are empirically related [34,35]. A systematic analysis was carried out to determine if the increase in Young's modulus is due to nucleation of CuO or due to variation in the composition of the matrix. The overall Young's modulus (E_c) was calculated using the following rule of mixtures expression,

$$E_c = fE_{CuO} + (1-f)E_{ESO} \quad (6)$$

where f is the volume fraction of the nucleated CuO, E_{CuO} is the Young's modulus of the CuO obtained from the literature [36] and E_{ESO} is the measured Young's modulus of the entropy stabilized oxide. The volume fraction of the nucleated CuO was calculated using the weight fraction of the CuO determined using Rietveld refinement. The overall Young's modulus (E_c) was calculated to be 131.6 GPa, 131.4 GPa and 131.2 GPa

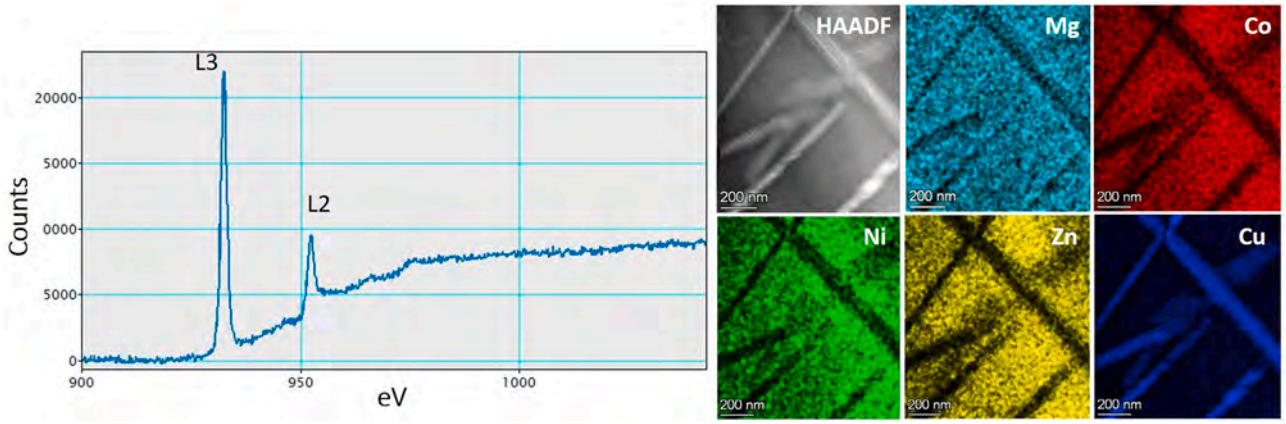

Fig. 10. shows the electron energy loss spectroscopy (EELS), high-angle annular dark-field imaging (HAADF) and STEM-EDS mapping of the CuO precipitates.

for ESO SC-5, ESO SC-2 and ESO SC-1, respectively. There is no significant variation observed in the calculated elastic modulus values when compared to the measured Young's modulus, as shown in Fig. 4(a). Therefore, the possibility of an increase in Young's modulus due to an increase in volume fraction of CuO nucleated can be ruled out.

The other possible reason for the increase in Young's modulus could be due to the variation in the atomic packing density of the material. Several reports highlight the relation between elastic constants of material and the atomic packing density (C_g). For the materials with the same composition and initial crystal structure but subjected to treatments affecting the packing density of material (annealing treatments for structure relaxation, high-pressure experiments), the elastic constants vary [37–40]. However, in this case, both the composition and initial structure varies with the cooling rate. Therefore, it can be concluded that it is not the material's atomic packing density (Cg) that influences the variation in Young's modulus.

The results show that the Young's modulus approach that of a 4-component system (ESO 4 C – No Cu^{2+} cations in the lattice) with a decrease in cooling rate. Therefore, it can be proposed that the variation in the observed properties is a result of a change in the chemical composition of the matrix and with an increase in CuO nucleation, the system behaves more like a CuO-free 4-component system. To concur with this observation, the matrix composition determined from the multivariate statistical analysis (MSA) on a STEM-EDX mapping of the sample ESO SC-1 is similar to that of the 4 component system - ESO 4 C (*refer to Section 4.1*). To further support the findings, the lattice parameter of the ESO SC-1 sample also approaches close to that of the ESO 4 C sample (*refer to* Fig. 8(b)). Therefore, the observed increase in Young's modulus of the material is solely because of the variation in the composition of the matrix with a decrease in cooling rate which answers the variation in hardness values as well.

4.2.2. Coefficient of thermal expansion

Similar to the mechanical properties, the material's linear thermal expansion coefficient (CTE) also shows variation with a decrease in cooling rate. The average CTE values reported for all the samples were calculated between 200 and 700 °C. It was because the ESO SC-5, ESO SC-2 and ESO-1 show a sharp transition beyond 700 °C. This can be attributed to the dissolution of CuO back into the rocksalt structure as the temperature is increased, which correlates with the transformation of a multi-phase mixture into a single-phase solid solution. The average CTE calculated between 900 and 1000 °C for the ESO SC-5, ESO SC-2 and ESO SC-1 sample agrees well with the average CTE value of the ESO stabilized sample, confirming that the dissolution of CuO has resulted in the formation of a single-phase rocksalt structure. Similar to the mechanical properties, the decrease in average CTE values with a decrease in cooling rate can therefore be attributed to the change in the chemical composition of the matrix. Also, the inverse relationship between the coefficient of thermal expansion and Young's modulus for all five samples (ESO 5C, ESO SC-5, ESO SC-2, ESO-1 and ESO 4C) follow the empirical relation of Barker et al.[34].

4.3. Effect of CuO nucleation on the properties

4.3.1. Thermal conductivity

Unlike the mechanical properties and coefficient of thermal expansion, the thermal conductivity does not vary significantly with variation in the composition of the matrix.

The 5-component entropy stabilized oxide has an amorphous-like thermal conductivity trend with temperature. The strong reduction in thermal conductivities for these five-cation oxides is attributed to the mass, charge disorder, and the variation in the interatomic force constants arising from different cations in the system [7,41,42]. Therefore, it was expected that with the composition of the matrix becoming more like a 4-component system with a decrease in cooling rate, the average thermal conductivity values would increase; however, this is not the case. The thermal conductivity of the material did not vary with the cooling rate. It was suspected that the other phenomena that occur with a decrease in cooling rate, i.e., nucleation of CuO precipitates should have contributed to this effect.

From Fig. 8(a), one noticeable difference observed for the slow cooled ESO samples is the peak broadening of the high intense peak of the ESO phase. One of the possible reasons for the peak broadening is that the grain size reduces with an increase in CuO nucleation and could be considered one of the reasons for hindering the increase in thermal conductivity [43,44]. However, Braun et al. [7] in their work concluded that for this particular ESO material, the phonons contributing to thermal conductivity have mean free paths less than the average grain size (150 nm) and that the contribution from grain boundaries is negligible. Therefore, it can be inferred that some other phenomenological changes in the system hamper the increase in average thermal conductivity values with an increase in CuO nucleation.

Therefore, to understand further, molecular dynamics (MD) simulations were carried out using the microstructural data obtained from HRTEM characterization. The details of the simulations are given in the supplementary information.

MD simulations reported in the literature show that charge disorder, mass disorder and variations in interatomic force constants all play a critical role in reducing the thermal conductivity of entropy stabilized oxide systems [7,8,41]. Taking into account these factors, the thermal conductivity for the ESO 5C and ESO 4C systems were calculated to be 12.9 W/mK and 15.7 W/mK @ 300 K, respectively. It is difficult to carry out precipitation simulations in molecular dynamics since the simulation times are very short [19,45]. Therefore, CuO precipitates of varying weight percentage was constructed and embedded into the matrix to understand the effect of CuO nucleation on thermal conductivity. Fig. 11

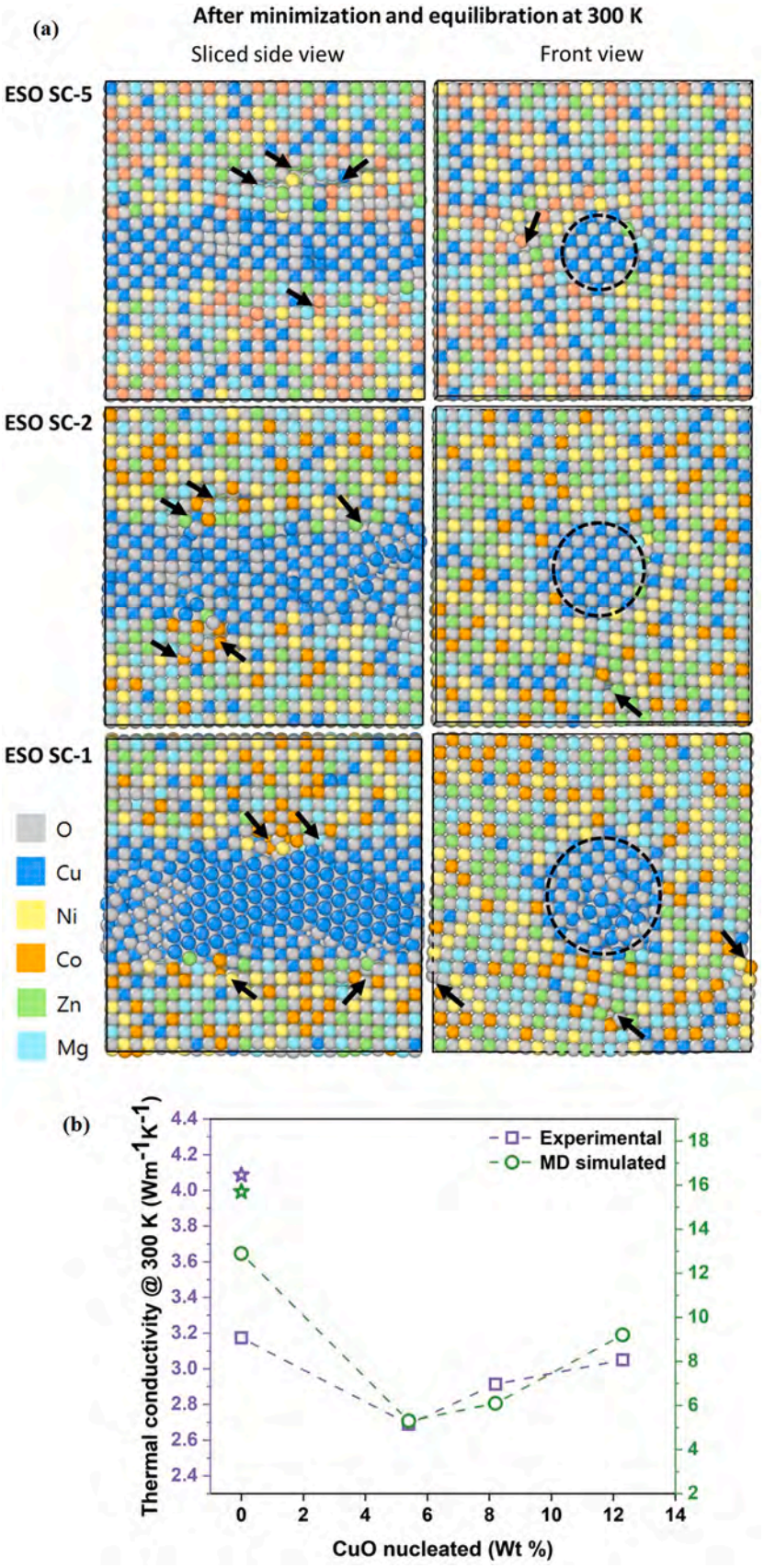

Fig. 11. **(a)** shows the matrix with varying wt% of CuO nucleated after minimization and equilibration at 300 K. Also observed is the creation of line defects in the matrix after equilibration, indicated by black arrows. The dotted black circle indicates the CuO precipitate. **(b)** shows the measured and MD calculated thermal conductivities at 300 K. For reference the values of ESO 4C system (no CuO) is represented by a star symbol.

(a) shows the matrix with different weight percentages of CuO precipitates before and after minimization and equilibration at 300 K. The corresponding thermal conductivities were calculated to be 5.3 W/mK, 6.1 W/mK and 9.2 W/mK @ 300 K for ESO SC-5, ESO SC-2 and ESO SC-1, respectively. Though the absolute values do not match the experimentally obtained thermal conductivity values, the relative trend is evident in Fig. 11 (b). The difference in the thermal conductivity values is because the interatomic force fields used to model the cation-anion interactions and thereby calculate thermal conductivity, are accurately parameterized only for Mg^{2+}-O^{2-} interactions and not for other cation-anion interactions [41,46]. From Fig. 11(a), it can be observed that there is direct evidence of line defects such as dislocations present in the ESO matrix (marked with black arrows), which contains CuO precipitate. Further confirmation of the presence of dislocations was obtained from neutron diffraction data. It can be seen from Fig. S3 that for the ESO SC-5, ESO SC-2 and ESO SC-1 systems, a distinct broadening of the elastic peaks is observed while the peaks remain fairly symmetrical. There are two reasons for the observed broadening of the main elastic peaks, the first is the size effect, and the second is the presence of defects (primarily dislocations) [47]. Microstructural analysis shows that the grain sizes do not vary significantly with the heat-treatment conditions. Therefore, the broadening of the peaks can solely be attributed to the presence of dislocations in the lattice.

The reduction in lattice thermal conductivity due to line defects is a well-studied phenomenon in literature [48–51]. Therefore, we believe that the negligent difference observed in the thermal conductivity values with an increase in CuO nucleation might be due to such defects in the lattice. The increase in thermal conductivity that is expected due to the decrease in the number of cations in the matrix should have been counteracted by the presence of defects created from CuO nucleation.

Phonons are the dominant heat carriers in non-metals and a reduction in elastic modulus is accompanied by a decrease in phonon group velocities and energies; as a result, a reduction in thermal conductivity [7]. However, in this case, though the elastic modulus increased by 33%, there is no apparent variation in the measured thermal conductivity values. Such phenomena have been observed by researchers previously in other material systems and were attributed to microstructural effects [52,53]. The possibility of increasing the material's elastic modulus without altering the thermal conductivity has much wider engineering benefits for the purpose of thermal barrier coatings and thermoelectrics [7].

4.3.2. *Fracture toughness*

The other property that have been influenced by the nucleation of CuO is the material's fracture toughness. CuO precipitates seem to have acted as an effective restraint on crack propagation and might have enhanced the fracture toughness of the *slow cooled* ESO samples. SEM imaging on one of the radial cracks was carried out for the ESO SC-1 sample. Fig. 12(a) shows the SEM micrographs of radial cracks observed on the sample surface after indentation and also shown, is a higher magnification of the radial crack hindered by the CuO precipitates. Fig. 12(b) shows the elemental EDS mapping of the constituent elements and it can be confirmed from the Cu elemental map that the obstacles in the path of the crack front are indeed CuO precipitates. It can be clearly seen that the CuO precipitates act as transitory obstacles for the propagating crack front. Instead of crack deflection, the crack propagates by breaking the CuO precipitates, thereby suggesting that the interface between the matrix and the precipitate is strong. In addition to CuO precipitates acting as transitory obstacles, the internal stresses arising from the difference in thermal expansion between the precipitate and matrix may also contribute to the toughening process [54].

Therefore, similar to the material's thermal conductivity, the fracture toughness of the material has also benefitted from CuO nucleation.

5. Conclusions

The following conclusions can be drawn from the present work.

- A successful approach is identified in altering the phase composition of (MgNiCoCuZn)O multicomponent oxides by varying the thermal post-treatment parameters. The control over the fraction of the secondary phase nucleated provides an additional degree of freedom to customize the material behavior.
- The change in the microstructure and elemental composition of the ESO system is ruled by the amount of CuO nucleated, which provides

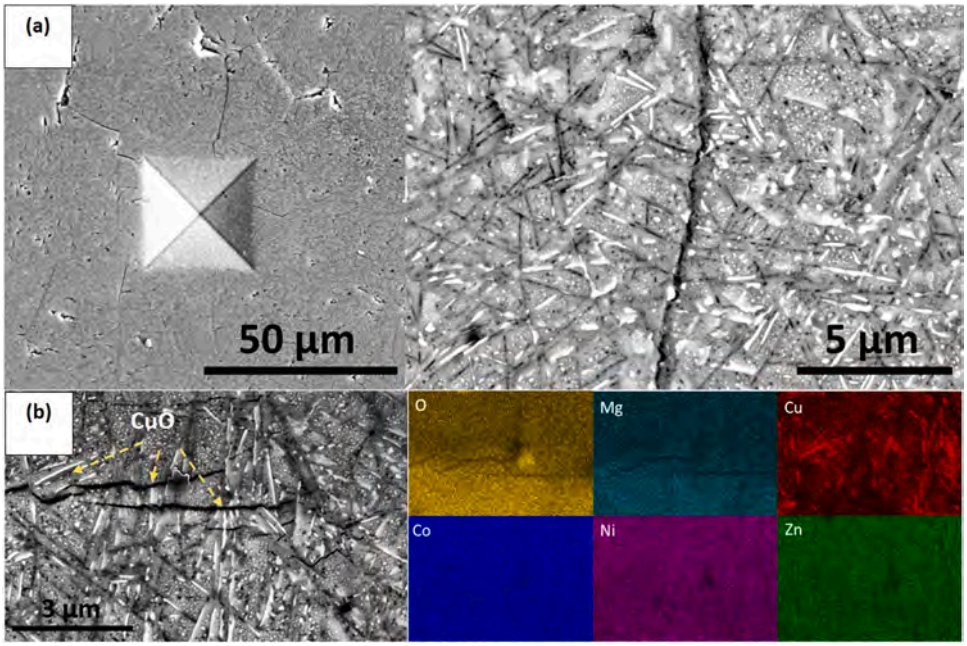

Fig. 12. **(a)** shows the SEM image of the radial cracks cracks observed on the ESO SC-1 sample surface after indentation and also shown is a higher magnification of the radial crack hindered by the CuO precipitates **(b)** shows the elemental EDS mapping of the constituent elements and it can be confirmed that the obstacles in the path of the crack front are indeed CuO precipitates.

an advantage of maintaining the structural complexity of a 5-component system but a performance equivalent to the 4-component system. All these microstructural and compositional changes in the system being reversible with temperature is an added benefit.

- The mechanical and thermal properties of the 5-component ESO system was studied for the first time as a function of varying cooling rates. For the slowest cooling rate, i.e., ESO SC-1, the Young's modulus, hardness and fracture toughness of the material increased by 33%, 26% and 15%, respectively, compared to the ESO 5C sample. At the same time, the Poisson's ratio and coefficient of thermal expansion of the material decreased by 6% and 34%. Unlike the other properties, the material's thermal conductivity did not vary with variation in cooling rate.
- The variation in material's Young's modulus, hardness and coefficient of thermal expansion with the decrease in cooling rate was attributed to the variation in the chemical composition of the matrix. With the decrease in cooling rate, the amount of CuO nucleated increased and the matrix composition was similar to that of an ESO 4C system (4-component system without Cu^{2+} ions in the matrix). As a result, the Young's modulus, hardness and linear coefficient of thermal expansion values for a 5-component ESO stabilized system approached that of an ESO 4C system with the decrease in cooling rate.
- The variation in fracture toughness and the negligent change in thermal conductivity values were attributed to CuO nucleation. With an increase in CuO nucleation, more lattice defects are formed in the lattice. The increase in thermal conductivity that was expected due to the decrease in the number of cations in the matrix was counteracted by the presence of defects created from CuO nucleation. The CuO precipitates also act as transitory obstacles and help improve the material's fracture toughness.

Declaration of Competing Interest

The authors declare that they have no known competing financial interests or personal relationships that could have appeared to influence the work reported in this paper.

Acknowledgements

The authors would like to gratefully acknowledge the X-ray diffraction and electron microscopy instrumentation facilities maintained by the Department of Metallurgical and Materials Engineering, IIT Madras. The authors thank sophisticated analytical instrument facility (SAIF), IIT Madras for the analytical support. The authors are thankful to Professor Pijush Ghosh and Dr. Payel Bandyopadhyay, IIT Madras for access to the nanoindentation facility. The authors would like to thank the Center for Non-Destructive Evaluation, IIT Madras for providing access to ultrasonic resonant frequency testing rig. The authors thank the Department of Physics, IIT Madras for the access to Raman Spectroscopy facility. The authors also thank the Physical Metallurgy Lab at IIT Madras for access to the microindentation facility. The authors would like to gratefully thank Karlsruhe Nano Micro Facility (Proposal-ID: 2021–025–030110) for their help and support in performing the high-resolution transmission electron microscopy (HR-TEM) measurements. The funding received from the Institute of Eminence Research Initiative Project on Materials and Manufacturing for Futuristic Mobility (project no. SB20210850MMMHRD008275) is gratefully acknowledged. The authors sincerely thank research scholars at Laboratory for High Performance Ceramics in IIT Madras, for their assistance, support and scientific inputs.

Appendix A. Supporting information

Supplementary data associated with this article can be found in the online version at doi:10.1016/j.jeurceramsoc.2023.03.016.

References

[1] C.M. Rost, E. Sachet, T. Borman, A. Moballegh, E.C. Dickey, D. Hou, J.L. Jones, S. Curtarolo, J. Maria, Entropy-stabilized oxides, Nat. Commun. 6 (2015) 1–8, https://doi.org/10.1038/ncomms9485.
[2] J. Gild, Y. Zhang, T. Harrington, S. Jiang, T. Hu, M.C. Quinn, W.M. Mellor, N. Zhou, K. Vecchio, J. Luo, High-entropy metal diborides: a new class of high-entropy materials and a new type of ultrahigh temperature ceramics, Sci. Rep. 6 (2016) 2–11, https://doi.org/10.1038/srep37946.
[3] T. Jin, X. Sang, R.R. Unocic, R.T. Kinch, X. Liu, J. Hu, H. Liu, S. Dai, Mechanochemical-assisted synthesis of high-entropy metal nitride via a soft urea strategy, Adv. Mater. 30 (2018) 1–5, https://doi.org/10.1002/adma.201707512.
[4] R.Z. Zhang, F. Gucci, H. Zhu, K. Chen, M.J. Reece, Data-driven design of ecofriendly thermoelectric high-entropy sulfides, Inorg. Chem. 57 (2018) 13027–13033, https://doi.org/10.1021/acs.inorgchem.8b02379.
[5] E. Castle, T. Csanádi, S. Grasso, J. Dusza, M. Reece, Processing and properties of high-entropy ultra-high temperature carbides, Sci. Rep. 8 (2018) 1–12, https://doi.org/10.1038/s41598-018-26827-1.
[6] C.M. Rost, E. Sachet, T. Borman, A. Moballegh, E.C. Dickey, D. Hou, J.L. Jones, S. Curtarolo, J. Maria, Entropy-stabilized oxides, Nat. Commun. (2015), https://doi.org/10.1038/ncomms9485.
[7] Jeffrey L. Braun, J.-P.M. Christina, M. Rost, Mina Lim, Ashutosh Giri, David H. Olson, George N. Kotsonis, Gheorghe Stan, Donald W. Brenner, P.E. Hopkins, Charge-induced disorder controls the thermal conductivity of entropy-stabilized oxides, Adv. Mater. 30 (2018) 1805004, https://doi.org/10.1002/adma.201805004.
[8] A. Giri, J.L. Braun, P.E. Hopkins, Reduced dependence of thermal conductivity on temperature and pressure of multi-atom component crystalline solid solutions, J. Appl. Phys. 123 (2018), https://doi.org/10.1063/1.5010337.
[9] K.C. Pitike, A.E. Marquez-Rossy, A. Flores-Betancourt, D.X. Chen, K.C. Santosh, V. R. Cooper, E. Lara-Curzio, On the elastic anisotropy of the entropy-stabilized oxide (Mg, Co, Ni, Cu, Zn)O compound, J. Appl. Phys. 128 (2020), https://doi.org/10.1063/5.0011352.
[10] D. Bérardan, S. Franger, D. Dragoe, A.K. Meena, N. Dragoe, Colossal dielectric constant in high entropy oxides, Phys. Status Solidi 333 (2016) 328–333, https://doi.org/10.1002/pssr.201600043.
[11] H. Chen, J. Fu, P. Zhang, H. Peng, C.W. Abney, K. Jie, X. Liu, M. Chi, S. Dai, Entropy-stabilized metal oxide solid solutions as CO oxidation catalysts with high-temperature stability, J. Mater. Chem. A 6 (2018) 11129–11133, https://doi.org/10.1039/c8ta01772g.
[12] S. Zhai, J. Rojas, N. Ahlborg, K. Lim, M.F. Toney, H. Jin, C. Chueh, A. Majumdar, Environmental Science The use of poly-cation oxides to lower the temperature of two-step thermochemical water splitting †, Energy Environ. Sci. (2018) https://doi.org/10.1039/c8ee00050f.
[13] A. Sarkar, L. Velasco, D. Wang, Q. Wang, G. Talasila, L. de Biasi, C. Kübel, T. Brezesinski, S.S. Bhattacharya, H. Hahn, B. Breitung, High entropy oxides for reversible energy storage, Nat. Commun. 9 (2018) 3400, https://doi.org/10.1038/s41467-018-05774-5.
[14] D. Bérardan, S. Franger, A.K. Meena, N. Dragoe, Room temperature lithium superionic conductivity in high entropy oxides, J. Mater. Chem. A 4 (2016) 9536–9541, https://doi.org/10.1039/c6ta03249d.
[15] G. Anand, A.P. Wynn, C.M. Handley, C.L. Freeman, Acta Materialia Phase stability and distortion in high-entropy oxides, Acta Mater. 146 (2018) 119–125, https://doi.org/10.1016/j.actamat.2017.12.037.
[16] Z. Rak, C.M. Rost, M. Lim, P. Sarker, C. Toher, S. Curtarolo, J.P. Maria, D. W. Brenner, Charge compensation and electrostatic transferability in three entropy-stabilized oxides: Results from density functional theory calculations, 095105-1–11, J. Appl. Phys. 120 (2016), https://doi.org/10.1063/1.4962135.
[17] C.M. Rost, Z. Rak, D.W. Brenner, J.-P. Maria, Local structure of the MgxNixCoxCuxZnxO(x=0.2) entropy-stabilized oxide: An EXAFS study, J. Am. Ceram. Soc. 100 (2017).
[18] D. Berardan, A.K. Meena, S. Franger, C. Herrero, N. Dragoe, Controlled Jahn-Teller distortion in (MgCoNiCuZn)O-based high entropy oxides, J. Alloy. Compd. 704 (2017) 693–700, https://doi.org/10.1016/j.jallcom.2017.02.070.
[19] L.K. Bhaskar, V. Nallathambi, R. Kumar, Critical role of cationic local stresses on the stabilization of entropy-stabilized transition metal oxides, J. Am. Ceram. Soc. 103 (2020) 3416–3424, https://doi.org/10.1111/jace.17029.
[20] J. Kaufman, K. Esfarjani, Tunable lattice distortion in MgCoNiCuZnO5 entropy-stabilized oxide, J. Mater. Res 36 (2021) 1615–1623, https://doi.org/10.1557/s43578-021-00198-2.
[21] M. Reda, A. Sarkar, S. Harsha, S.S. Bhattacharya, B. Breitung, H. Hahn, L. Velasco, Scripta Materialia On the homogeneity of high entropy oxides: An investigation at the atomic scale, Scr. Mater. 166 (2019) 58–63, https://doi.org/10.1016/j.scriptamat.2019.02.039.
[22] B. Yue, W. Dai, X. Zhang, H. Zhang, W. Zhong, Scripta Materialia Deformation behavior of high-entropy oxide (Mg, Co, Ni, Cu, Zn) O under extreme compression, Scr. Mater. 219 (2022), 114879, https://doi.org/10.1016/j.scriptamat.2022.114879.
[23] J. Chen, W. Liu, J. Liu, X. Zhang, M. Yuan, Y. Zhao, J. Yan, M. Hou, J. Yan, M. Kunz, N. Tamura, H. Zhang, Z. Yin, Stability and Compressibility of Cation-Doped High-Entropy Oxide, (2019). https://doi.org/10.1021/acs.jpcc.9b04992.
[24] A.D. Dupuy, X. Wang, J.M. Schoenung, Entropic phase transformation in nanocrystalline high entropy oxides, Mater. Res. Lett. 7 (2019) 60–67, https://doi.org/10.1080/21663831.2018.1554605.

[25] A.D. Dupuy, M.R. Chellali, H. Hahn, J.M. Schoenung, Multiscale phase homogeneity in bulk nanocrystalline high entropy oxides, J. Eur. Ceram. Soc. 41 (2021) 4850–4858, https://doi.org/10.1016/j.jeurceramsoc.2021.03.035.
[26] A.D. Dupuy, I.T. Chiu, P. Shafer, E. Arenholz, Y. Takamura, J.M. Schoenung, Hidden transformations in entropy-stabilized oxides, J. Eur. Ceram. Soc. 41 (2021) 6660–6669, https://doi.org/10.1016/j.jeurceramsoc.2021.06.014.
[27] A. Balagurov, D. Balagurov, I. Bobrikov, A. Bogdzel, V. Drozdov, A. Kirilov, V. Kruglov, S. Kulikov, S. Murashkevich, V. Prikhodko, V. Shvetsov, V. Simkin, A. Sirotin, N. Zernin, V. Zhuravlev, Nuclear Inst. and Methods in Physics Research B High-resolution neutron Fourier diffractometer at the IBR-2 pulsed reactor: a new concept, Nucl. Inst. Methods Phys. Res. B 436 (2018) 263–271, https://doi.org/10.1016/j.nimb.2018.09.045.
[28] J. Rodriguez-carvajal, Recent advances in magnetic structure determination by neutron powder diffraction, Phys. B Condens. Matter 192 (1993) 55–69.
[29] S. Stoll, A. Schweiger, EasySpin, a comprehensive software package for spectral simulation and analysis in EPR, J. Magn. Reson 178 (2006) 42–55, https://doi.org/10.1016/j.jmr.2005.08.013.
[30] N.J. Usharani, A. Bhandarkar, S. Subramanian, S.S. Bhattacharya, Antiferromagnetism in a nanocrystalline high entropy oxide (Co,Cu,Mg,Ni,Zn)O: Magnetic constituents and surface anisotropy leading to lattice distortion, Acta Mater. 200 (2020) 526–536, https://doi.org/10.1016/j.actamat.2020.09.034.
[31] D. Berardan, A.K. Meena, S. Franger, C. Herrero, N. Dragoe, Controlled Jahn-Teller distortion in (MgCoNiCuZn) O-based high entropy oxides, J. Alloy. Compd. 704 (2017) 693–700, https://doi.org/10.1016/j.jallcom.2017.02.070.
[32] C.M. Parish, L.N. Brewer, Multivariate statistics applications in phase analysis of STEM-EDS spectrum images, Ultramicroscopy 110 (2010) 134–143, https://doi.org/10.1016/j.ultramic.2009.10.011.
[33] N.J. Long, A.K. Petford-Long, In-situ electron-beam-induced reduction of CuO: a study of phase transformations in cupric oxide, Ultramicroscopy 20 (1986) 151–159, https://doi.org/10.1016/0304-3991(86)90181-6.
[34] R.E. Barker, An approximate relation between elastic moduli and thermal expansivities, J. Appl. Phys. 34 (1963) 107–116, https://doi.org/10.1063/1.1729049.
[35] X.Q. Chen, H. Niu, D. Li, Y. Li, Modeling hardness of polycrystalline materials and bulk metallic glasses, Intermetallics 19 (2011) 1275–1281, https://doi.org/10.1016/j.intermet.2011.03.026.
[36] J.K. Lumpp, N. Chen, K.C. Goretta, H.M. Herro, Mechanical properties of CuO, High. Temp. Mater. Process 9 (1990) 1–6, https://doi.org/10.1515/HTMP.1990.9.1.1.
[37] S.M. Antao, C.J. Benmore, B. Li, L. Wang, E. Bychkov, J.B. Parise, Network rigidity in GeSe2 glass at high pressure, Phys. Rev. Lett. 100 (2008) 2–5, https://doi.org/10.1103/PhysRevLett.100.115501.
[38] C. Zha, R.J. Hemley, H. Mao, T.S. Duffy, C. Meade, Acoustic velocities and refractive index of SiO2 glass to 57.5 GPa by Brillouin scattering, Phys. Rev. B 50 (1994) 13105–13112. ⟨http://link.aps.org/doi/10.1103/PhysRevB.50.13105⟩.
[39] J. Nicholas, S. Sinogeikin, J. Kieffer, J. Bass, A high pressure Brillouin scattering study of vitreous boron oxide up to 57GPa, J. Non Cryst. Solids 349 (2004) 30–34, https://doi.org/10.1016/j.jnoncrysol.2004.08.258.
[40] G.N. Greaves, A.L. Greer, R.S. Lakes, T. Rouxel, Poisson's ratio and modern materials, Nat. Mater. 10 (2011) 823–837, https://doi.org/10.1038/nmat3134.
[41] M. Lim, Z. Rak, J.L. Braun, C.M. Rost, G.N. Kotsonis, P.E. Hopkins, J.P. Maria, D. W. Brenner, Influence of mass and charge disorder on the phonon thermal conductivity of entropy stabilized oxides determined by molecular dynamics simulations, J. Appl. Phys. 125 (2019), https://doi.org/10.1063/1.5080419.
[42] A. Giri, J.L. Braun, C.M. Rost, P.E. Hopkins, On the minimum limit to thermal conductivity of multi-atom component crystalline solid solutions based on impurity mass scattering, Scr. Mater. 138 (2017) 134–138, https://doi.org/10.1016/j.scriptamat.2017.05.045.
[43] W.D. KINGERY, M.C. McQUARRIE, Thermal conductivity: I, Concepts of measurement and factors affecting thermal conductivity of ceramic materials, J. Am. Ceram. Soc. 37 (1954) 67–72, https://doi.org/10.1111/j.1551-2916.1954.tb20100.x.
[44] H. Dong, B. Wen, R. Melnik, Relative importance of grain boundaries and size effects in thermal conductivity of nanocrystalline materials, Sci. Rep. 4 (2014) 7037, https://doi.org/10.1038/srep07037.
[45] S. Xiao, Y. Kong, Y. Qiu, Y. Du, The microstructure evolution of U1 and U2 nanowires constrained in Al matrix, Comput. Mater. Sci. 117 (2016) 180–187, https://doi.org/10.1016/j.commatsci.2016.01.028.
[46] P. Shukla, T. Watanabe, J.C. Nino, J.S. Tulenko, S.R. Phillpot, Thermal transport properties of MgO and Nd2Zr2O7 pyrochlore by molecular dynamics simulation, J. Nucl. Mater. 380 (2008) 1–7, https://doi.org/10.1016/j.jnucmat.2008.06.043.
[47] T. Ungár, I. Dragomir, Á. Révész, A. Borbély, The contrast factors of dislocations in cubic crystals: the dislocation model of strain anisotropy in practice, J. Appl. Crystallogr 32 (1999) 992–1002, https://doi.org/10.1107/S0021889899009334.
[48] K. Termentzidis, M. Isaiev, A. Salnikova, I. Belabbas, D. Lacroix, J. Kioseoglou, Impact of screw and edge dislocations on the thermal conductivity of individual nanowires and bulk GaN: a molecular dynamics study, Phys. Chem. Chem. Phys. 20 (2018) 5159–5172, https://doi.org/10.1039/c7cp07821h.
[49] Y. Cheng, M. Nomura, S. Volz, S. Xiong, Phonon-dislocation interaction and its impact on thermal conductivity, J. Appl. Phys. 130 (2021), https://doi.org/10.1063/5.0054078.
[50] S. Hu, H. Zhang, S. Xiong, H. Zhang, H. Wang, Y. Chen, S. Volz, Y. Ni, Screw dislocation induced phonon transport suppression in SiGe superlattices, Phys. Rev. B 100 (2019) 1–7, https://doi.org/10.1103/PhysRevB.100.075432.
[51] R.L. Sproull, M. Moss, H. Weinstock, Effect of dislocations on the thermal conductivity of lithium fluoride, J. Appl. Phys. 30 (159AD) (2015) 334–337, https://doi.org/10.1002/pssb.2221630134.
[52] J. Bourret, N. Tessier-Doyen, R. Guinebretiere, E. Joussein, D.S. Smith, Anisotropy of thermal conductivity and elastic properties of extruded clay-based materials: evolution with thermal treatment, Appl. Clay Sci. 116–117 (2015) 150–157, https://doi.org/10.1016/j.clay.2015.08.006.
[53] P.M. Nigay, T. Cutard, A. Nzihou, The impact of heat treatment on the microstructure of a clay ceramic and its thermal and mechanical properties, Ceram. Int. 43 (2017) 1747–1754, https://doi.org/10.1016/j.ceramint.2016.10.084.
[54] B. Lawn, Fracture of brittle solids, 2nd ed., Cambridge university press, 1993.